Journal of King Saud University - Computer and Information Sciences 36 (2024) 101900

HOSTED BY

Contents lists available at ScienceDirect

Journal of King Saud University - Computer and Information Sciences

journal homepage: www.sciencedirect.com

Full length article

Admittance swarm-based adaptive controller for lower limb exoskeleton with gait trajectory shaping

Mohammad Soleimani Amiri [a,b], Rizauddin Ramli [a,*]

[a] Department of Mechanical and Manufacturing Engineering, Faculty of Engineering and Built Environment, Universiti Kebangsaan Malaysia, 43600 Bangi, Selangor, Malaysia

[b] Department of Manufacturing Engineering Technology, Faculty of Industrial and Manufacturing Technology and Engineering, Universiti Teknikal Malaysia Melaka, 76100 Durian Tunggal, Melaka, Malaysia

ARTICLE INFO

MSC:
93A99
49N25

Keywords:
Beetle antenna searching
Adaptive controller
Admittance model
Exoskeleton

ABSTRACT

The motivation for developing a rehabilitation lower-limb exoskeleton robot was to provide functional robot-assisted therapy for assisting physiotherapists in improving hemiplegic patients' walking recovery. Rehabilitation tasks required robust and precise trajectory-tracking performance, mainly achieved with exoskeleton robots. This paper presents a study on the gait trajectory cycles of a rehabilitation lower-limb exoskeleton robot controlled by an Admittance Swarm Initialized Adaptive (ASIA). The aim of this paper was to develop a robust adaptive controller integrated with admittance model to overcome human–robot interaction forces generated by the wearer. The parameters of the ASIA controller were efficiently initialized using swarm beetle antenna searching. An experiment was conducted on a prototype lower limb exoskeleton with four degrees of freedom, involving a healthy human subject for gait trajectory analysis. The results demonstrated the effectiveness of the proposed method in terms of control performance, steady-state error reduction, and robustness. The statistical analysis revealed that the ASIA performed 63 %, 53 % and 48 % less in average error compared to adaptive conventional controllers used in the same exoskeleton platform. The findings ascertained the potential of the ASIA controller in improving human mobility through lower limb exoskeleton applications.

1. Introduction

Neurological diseases such as spinal cord injuries and strokes have been increasingly prevalent, serving as major causes of mobility restrictions and balance issues (Lee et al., 2022; Khadidos et al., 2023; Singh et al., 2023). To minimize the side effects of chronic diseases, the selection of appropriate rehabilitation training is crucial (Wang et al., 2022; Celesti et al., 2023). Recent clinical research on neurological rehabilitation suggests that engaging in repetitive motor activities has a beneficial effect on preserving movement functionality (Joel et al., 2022; Metzger et al., 2014).

In traditional rehabilitation programs, physiotherapists are responsible for delivering individualized manual treatments based on their expertise. Choosing the appropriate difficulty level and adapting exercises during physiotherapy can be challenging due to the subjective perception of trained therapists (Sabbahi et al., 2022). Nonetheless, the conventional rehabilitation process is labour-intensive and heavily dependent on the expertise of physiotherapists. Implementing conventional manual therapy often poses frequent challenges and requires significant effort from medical professionals, especially when caring for larger patients (Cortese et al., 2015).

In recent years, there has been an increase in the utilization of robotic rehabilitation devices. These devices enable repetitive rehabilitation treatment, which helps prevent muscle atrophy, enhances motor functions in disabled patients, and alleviates the physical burden on physiotherapists (Takebayashi et al., 2022). Robotic therapy, along with clinical rehabilitation treatments, offers an affordable and effective long-term treatment option that can potentially replace

* Corresponding author.
E-mail address: rizauddin@ukm.edu.my (R. Ramli).
Peer review under responsibility of King Saud University.

Production and hosting by Elsevier

https://doi.org/10.1016/j.jksuci.2023.101900
Received 27 June 2023; Received in revised form 18 October 2023; Accepted 22 December 2023
Available online 4 January 2024

Nomenclature

PSO	particle swarm optimization
ASIA	admittance swarm initialized adaptive
SBAS	swarm beetle antenna searching
LH	left hip
LK	left knee
RH	right hip
RK	right knee
M_I	virtual mass matrix
D_I	virtual damping matrix
K_I	virtual stiffness matrix
d	virtual displacement
f	measurable human–robot interaction force
k	joint index
L_k	distance of the force sensor
q_h	trajectory deviation
q_d	intended trajectory
q_r	reference trajectory
$J(.)$	Jacobian matrix
Y	end-position of the left and right legs
P_{rx}^H and P_{lx}^H	positions of the right and left hip in the sagittal direction
COM	center of mass
P_o	COM position
β and Γ	positive constant
ZMP	Zero Moment-Point
q, $\dot{q}$, and $\ddot{q}$	joint angle, joint angular velocity, and joint angular acceleration
$M(q)$	mass and inertia matrix
$V(q,\dot{q})$	centrifugal and Coriolis forces vector
$C(q)$	gravitational forces
$F_e(t)$	external disturbance forces
T	forces generated by the actuators
T_f	human–robot interaction force
X	state vector
A and B	system parameters matrices
u	control input
K_p, K_i, and k_d	controller parameters
e	steady-state error
q	actual trajectory
$\dot{Z}$	derivative of e
$V(x)$	Lyapunov function
P and Q	positive definite matrices
Ψ	adaptive rate
$\hat{K}_p$, $\hat{K}_i$, and $\hat{K}_d$	estimation of the controller parameters
$\acute{K}_p$, $\acute{K}_i$, and $\acute{K}_d$	unknown controller parameters
$e_{obj}(s)$	steady-state error of the objective function
x	design variables
$G_i(s)$	mathematical model of each joint
$f(x)$	objective function
$\vec{c}$	unit vector
a	randomly generated value between -1 and 1
n	denotes the number of design variables in SBAS
i	number of iteration of SBAS
j	population size of SBAS
x_r and x_l	positions of the right and left antennas
d^i	searching diameter at iteration i
λ^i	step size at iteration i
$f(x_l)$ and $f(x_r)$	objective function of left and right antenna positions
d	searching diameter
λ	step size
d_o	initial values of the searching diameter
ω_o	searching bias
$f_{best(x)}$	minimum value of the objective function
$g_{\text{best}}(x)$	global best
TP	True Positive
FN	True Negative
FP	False Positive
TN	True Negative

high-intensity and repetitive physical rehabilitation treatments (Zhang et al., 2023). However, human–robot interaction has not been considered in many walking exoskeletons. In addition, the adaptation of walking exoskeletons to the ground surface condition has been ignored in several scenarios. For instance, if there is an obstacle on the ground, the walking steps should be adjusted based on the obstacle size.

The field of robot-assisted systems has garnered significant attention from researchers as an important area within robotics, particularly for the rehabilitation of post-stroke patients (Gallagher et al., 2022). The utilization of lower limb rehabilitation exoskeleton robots has proven beneficial for individuals with muscle injuries and mobility issues. These robots aid in daily activities and contribute to the improvement of their motor skills (Liao et al., 2022). Hence, the exoskeleton robot plays a crucial role in supporting the user's joints and providing guidance in the desired direction. This allows users to perform exercises with minimal muscle activity and metabolism (Li et al., 2022). Accordingly, the exoskeleton robot plays a crucial role in supporting the user's joints and providing guidance in the desired direction. This allows users to perform exercises with minimal muscle activity and metabolism. Jiang et al. (2019) presented the effects of robot-assisted treatment for the upper limb, comparing it with traditional rehabilitation, during a two-week post-stroke physical therapy program.

Accomplishing precise tracking of limb joint movements with minimal long-term error and maintaining strong performance in the presence of disruptions and uncertainties is essential in the field of control systems. Developing effective control strategies for rehabilitation robots is essential to achieve satisfactory outcomes in various rehabilitation treatments (Shao and Fan, 2021; Daachi et al., 2015). Wu et al. (2018) developed a neural-fuzzy adaptive control scheme based on radial basis functions for a rehabilitation exoskeleton designed to assist human arm movement. Sun et al. (2021) proposed a reduced adaptive fuzzy decoupling control strategy for a lower limb exoskeleton. They designed a fuzzy inference system based on the steady-state behaviour of the control system and validated the approach on a multi-input-multi-output uncertain nonlinear system model. Liu et al. (2021) investigated a sliding mode control system for an upper-limb exoskeleton with pneumatic muscle joints. They developed a fast terminal sliding mode control approach incorporating a non-linear disturbance observer to address dynamic model errors and to handle load disturbances. Guo et al. (2022) studied model parametric identification for a lower limb exoskeleton, employing biogeography-based learning Particle Swarm Optimization (PSO) to determine the unknown parameters of the mathematical model. Additionally, they implemented an active admittance controller to enable accurate tracking of angular trajectories. By considering the above studies, we developed an adaptive controller that had its parameters initialized precisely by means of

Table 1
Literature analysis.

No.	Reference	Year	Method	Exoskeleton study
1	Wu et al. (2018)	2018	Neural-fuzzy adaptive control	Yes
2	Sun et al. (2021)	2021	Adaptive fuzzy controller	Yes
3	Liu et al. (2021)	2021	Sliding-mode controller	Yes
4	Guo et al. (2022)	2022	PSO	Yes
5	Wu and Chen (2023)	2023	Admittance controller	No
6	Xu et al. (2023)	2023	Admittance control	No
7	Cho et al. (2023)	2023	Admittance controller	No
8	Pulloquinga et al. (2023)	2023	Admittance controller	No

an optimization algorithm for the walking exoskeleton. As a result, the walking exoskeleton had both a robust and precise trajectory tracking.

Many researchers have shown considerable interest in the field of human–robot interaction (Mujica et al., 2023). One of the important interaction methods is the admittance model (Wang et al., 2023). Wu and Chen (2023) proposed a variable admittance time-delay control. A time-delay approximator is used to estimate the uncertain parameters without the exact knowledge about the dynamic model. Its sliding mode admittance controller is established to obtained objective admittance characteristics. Xu et al. (2023) presented an admittance controller for stable and unstable linear time-invariant systems based on human–robot interaction. Cho et al. (2023) developed an admittance control for human–robot interaction implemented in a dual-arm social robot. In their model the external torque and force external torques exerted by the user, as well as the robot's pose to control movement speed has been considered. Pulloquinga et al. (2023) studied an admittance controller for a parallel rehabilitation robot, which overcomes the limitations of singular configurations by using a real-time singularity avoidance algorithm. Their model was developed to adapt the controller with the external forces and torques applied by the patients. Motivated by the above studies, in which human intention had been considered, we integrated the human–robot interaction into a walking exoskeleton using the admittance model in this work. Therefore, the step trajectory was shaped while the human subject wore the exoskeleton. Table 1 illustrates the control strategies with different methods used in existing literature.

From the existing literature in Table 1, a number of control systems have been established to improve the robustness and stability of nonlinear systems, with more efficient tracking performance. However, the human–robot interaction and admittance controller have not been used for the exoskeleton controller. Therefore, the objective of this work was to develop a robust adaptive controller integrated with admittance model to overcome forces and torques applied to the control system by the wearer. The existing studies have addressed the robustness and stability of the control system for the exoskeleton. From the perspective of human–robot interaction, robustness and precision, the strategy for a lower limb exoskeleton it is needed to address all the issues simultaneously. The novelty of this paper was the development of an Admittance Swarm Initialized Adaptive (ASIA) controller to enhance gait trajectory cycles and to improve control performance for a walking lower-limb exoskeleton robot. This method was proposed to address issues regarding human–robot interaction, robustness, and precision of the control strategies for walking exoskeleton application. The contributions of this paper are as follows:

- The introduction of the utilization of an admittance model, which ensures that the walking exoskeleton robot follows the desired trajectory based on the human–robot forces generated by the wearer.
- The investigation of the novel ASIA controller, which combines swarm-based intelligence with an adaptive Lyapunov-based controller. The ASIA controller is specifically designed to enhance the performance and adaptability of the lower-limb exoskeleton robot.
- The initialization parameters of ASIA using Swarm Beetle Antenna Searching (SBAS), leading to efficient improvements in the control system's performance.

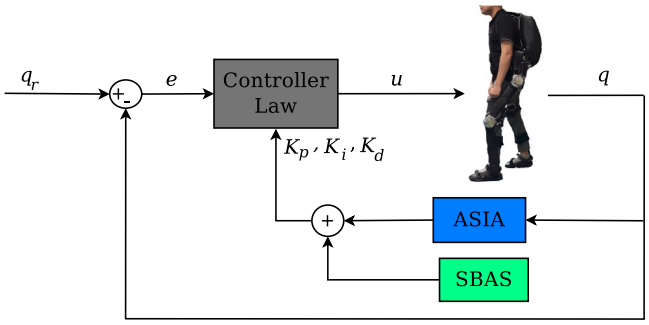

Fig. 1. Closed-loop diagram of ASIA controller.

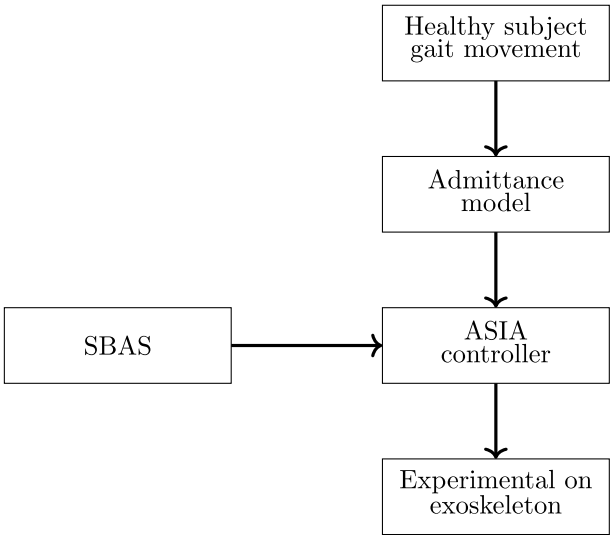

Fig. 2. Schematic representation of ASIA control system.

The rest of the paper has been organized as follows: Section 2 focuses on the development of the admittance adaptive control system and presents the mechanical and hardware structure of the lower limb exoskeleton. Section 3 provides details about the experimental platform and validation of the proposed control system. Finally, Section 4 concludes the paper.

2. Gait trajectory control design based on admittance swarm adaptive analysis

In this study, we have proposed a novel swarm-initialized adaptive controller called ASIA for controlling the angular joint trajectory of an exoskeleton. The objective of ASIA was to combine swarm-based intelligence, known as SBAS, with a Lyapunov-based adaptive controller to reduce the steady-state error of the joint angular trajectory within a specific range. The controller parameters were initially initialized using the SBAS optimization algorithm and subsequently adjusted based on the Lyapunov function to achieve accurate joint tracking of the desired trajectory. Fig. 1 illustrates the closed-loop diagram of the ASIA controller integrated with SBAS.

The schematic representation of the ASIA control system has been illustrated in Fig. 2.

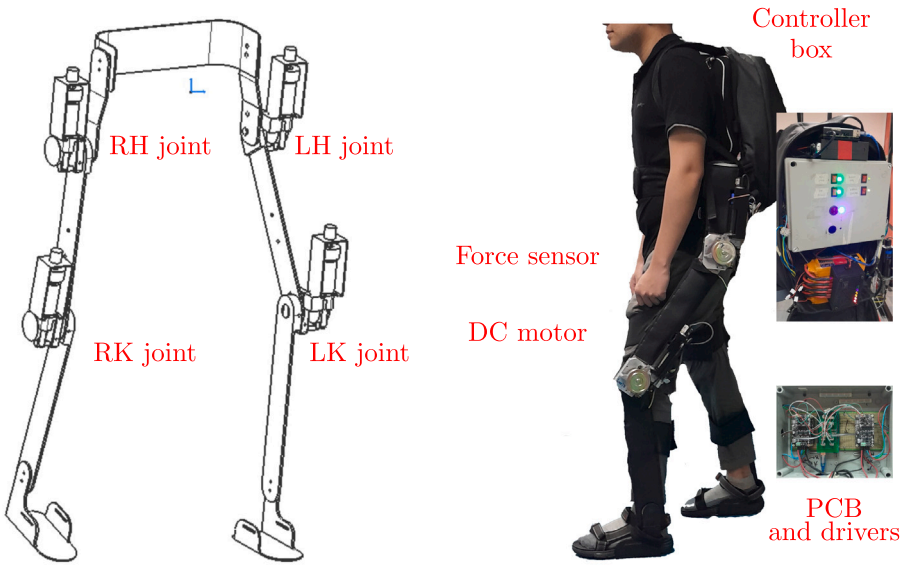

(a) Exoskeleton structure

(b) Hardware system

Fig. 3. System of the wearable lower limb exoskeleton.

Table 2
DoFs and motions of the wearable lower limb exoskeleton.

DoF	Motion	Property
LH & RH	flexion & extension	Active
LK & RK	flexion & extension	Active

2.1. Structure of exoskeleton system

The primary motivation of the gait training rehabilitation robot is to enhance the wearer's walking ability in daily life. Therefore, in this study, a prototype of a wearable lower limb exoskeleton with four degrees of freedom (DoF) was developed. The exoskeleton featured four active joints, comprising two hip joints (left hip — LH and right hip — RH) and two knee joints (left knee — LK and right knee — RK), for each leg. To facilitate the subsequent discussion in this paper, we will use the abbreviations LH, RH, LK, and RK to refer to the left hip, right hip, left knee, and right knee, respectively. The system of the wearable lower limb exoskeleton has been depicted in Fig. 3.

The thigh and shank links of the exoskeleton had lengths of 40 cm and 41 cm, respectively. Table 2 displays the motions and DoF of the wearable lower limb exoskeleton.

2.2. Hardware structure

The overall system was supported by an Intel® Core™ i3 processor computer with 16 GB RAM, which executed the control programs, ran the control strategy and provided a user interface for patient and physiotherapist interaction. Data acquisition was facilitated through WiFi, allowing the acquired data to be transmitted from the onboard processor to the PC. Diagrammatic representation of the wearable lower limb exoskeleton has been depicted in Fig. 4.

The onboard processor was connected to Arduino microprocessor board to process input and output of analogue signals from encoders, force sensors and actuators. The FSR402 force sensor, which was located in each joint was used to measure the human–robot interaction force. Fig. 5 represents the schematic diagram of the wearable lower limb exoskeleton.

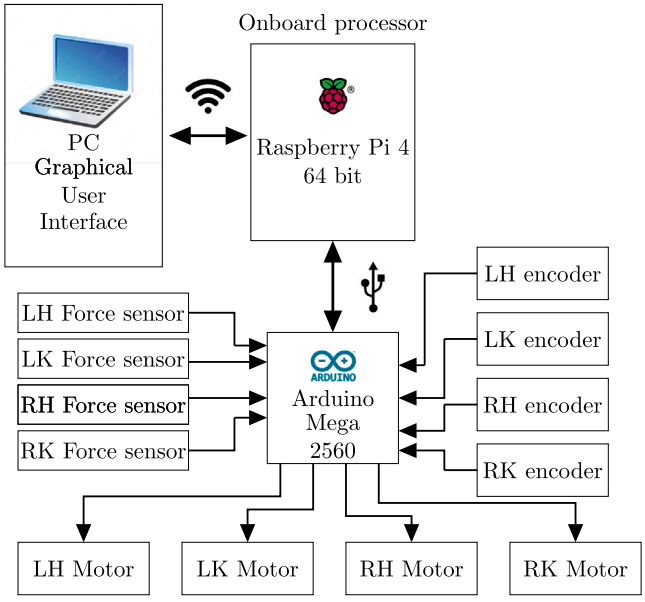

Fig. 4. Diagrammatic representation of the wearable lower limb exoskeleton.

2.3. Admittance-based gait trajectory shaping

In order to represent the effect of human force interaction on the exoskeleton, an admittance model of mass–damper–spring is determined as follows:

$$M_I \ddot{d} + D_I \dot{d} + K_I d = f \tag{1}$$

where $M_I = \text{diag}\begin{bmatrix} M_{I_1} & M_{I_2} & \dots & M_{I_n} \end{bmatrix} \in \mathbb{R}^{n\times n}$,
$D_I = \text{diag}\begin{bmatrix} D_{I_1} & D_{I_2} & \dots & D_{I_n} \end{bmatrix} \in \mathbb{R}^{n\times n}$, and
$K_I = \text{diag}\begin{bmatrix} K_{I_1} & K_{I_2} & \dots & K_{I_n} \end{bmatrix} \in \mathbb{R}^{n\times n}$ are positive definite matrices representing virtual mass, virtual damping, and virtual stiffness, respectively. Here, $d = \begin{bmatrix} d_1, d_2, \dots d_n \end{bmatrix}^T \in \mathbb{R}^n$ denotes the virtual displacement, and $f = \begin{bmatrix} f_1, f_2, \dots f_n \end{bmatrix}^T \in \mathbb{R}^n$ represents the measurable human–robot

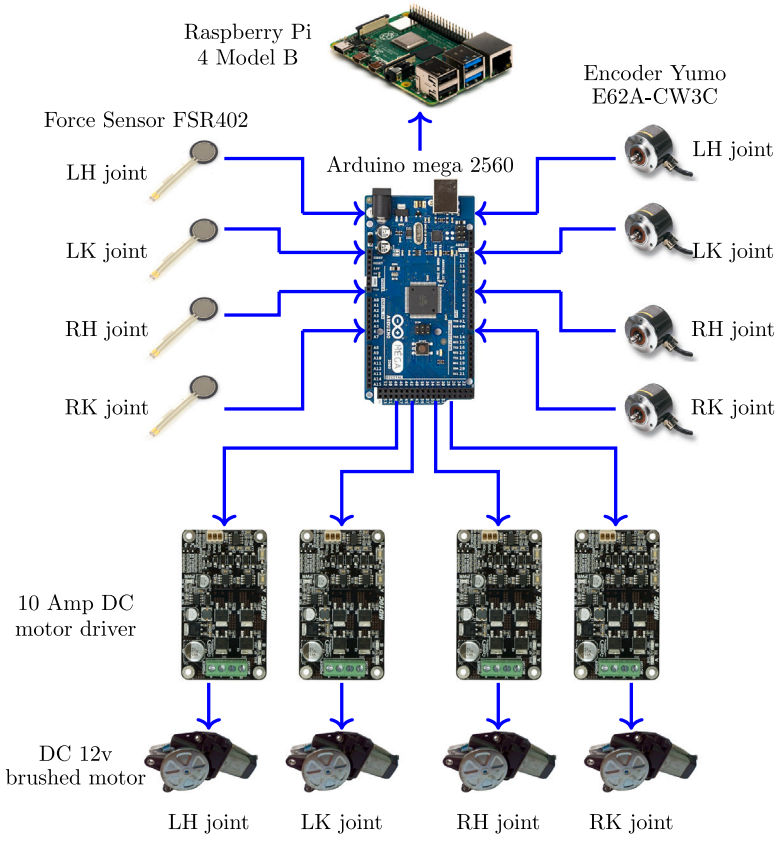

Fig. 5. Schematic diagram of the wearable lower limb exoskeleton.

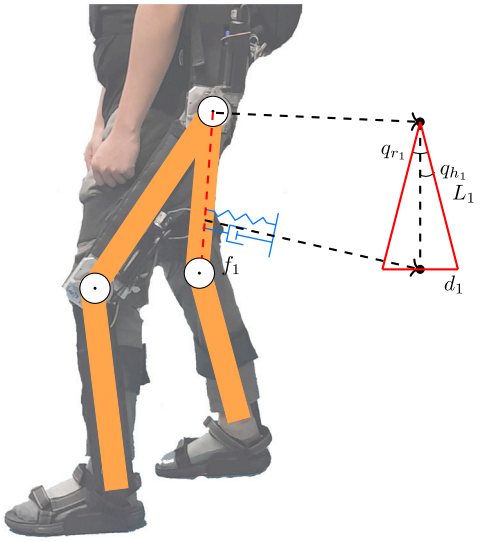

Fig. 6. Admittance model of the wearable lower limb exoskeleton.

interaction force. Eq. (1) is considered in one dimension as follows:

$$M_{I_k}\ddot{d_k} + D_{I_k}\dot{d_k} + K_{I_k}d_k = f_k \tag{2}$$

The position of d can be determined based on the given force f. Fig. 6 illustrates the admittance model of the lower exoskeleton.

Considering the admittance model, we can express the following equation:

$$\tan q_{h_k} \approx \frac{d_k}{L_k}, \quad k = 1, 2, \ldots, n \tag{3}$$

where k represents the joint index, L_k denotes the distance of the force sensor relative to the corresponding joint, and q_{h_k} represents the trajectory deviation between the wearer's intended trajectory q_{d_k} and the reference trajectory q_{r_k}:

$$q_{h_k} = q_{r_k} - q_{d_k} \tag{4}$$

In Eq. (4), $q_r = \begin{bmatrix} q_{r_1} & q_{r_2} & \ldots & q_{r_n} \end{bmatrix}^T$ represents the reference trajectory, $q_d = \begin{bmatrix} q_{d_1} & q_{d_2} & \ldots & q_{d_n} \end{bmatrix}^T$ denotes the wearer's intended trajectory, and $q_h = \begin{bmatrix} q_{h_1} & q_{h_2} & \ldots & q_{h_n} \end{bmatrix}^T$ represents the differences between the two trajectories. Based on Eq. (3), its time derivative can be expressed as follows:

$$\dot{d_k} = L_k \dot{q_{h_k}} \sec^2 q_{h_k} \tag{5}$$

$$\ddot{d_k} = L_k \left[\frac{2\dot{q_{h_k}} q_{h_k}}{\cos^3 q_{h_k}} + \ddot{q_{h_k}} \sec^2 q_{h_k} \right] \tag{6}$$

By substituting Eqs. (5) and (6) into Eq. (3), we obtain:

$$\mathbb{M}_{l_k}\ddot{q_{h_k}} + \mathbb{D}_{l_k}\dot{q_{h_k}} + \mathbb{K}_{l_k} = f_k \tag{7}$$

where

$$\mathbb{M} = M_{I_i} L_k \sec q_{h_k} \tag{8}$$

$$\mathbb{D} = L_k \left[\frac{2 \sin q_{h_k}}{\cos^3 q_{h_k}} + D_{I_k} \sec^2 q_{h_k} \right] \tag{9}$$

$$\mathbb{K} = L_k K_{I_k} \tan q_{h_k} \tag{10}$$

By substituting Eq. (4) into Eq. (7), we obtain:

$$\mathbb{M}_{l_k}(\ddot{q_{h_k}} + \ddot{q_{r_k}}) + \mathbb{D}_{l_k}(\dot{q_{h_k}} + \dot{q_{r_k}}) + \mathbb{K}_{l_k} = f_k \tag{11}$$

By applying the Jacobian matrix to obtain the transformation equation, we can express it as follows:

$$\dot{q}_r = J^{+}(q_r)\dot{X} \tag{12}$$

$$\ddot{q}_r = \dot{J}^{+}(q_r)\dot{X} + J^{+}(q_r)\ddot{X} \tag{13}$$

Here, $J(q_r)$ represents the Jacobian matrix. $Y = \begin{bmatrix} P_{rx} & P_{ry} & P_{lx} & P_{ly} \end{bmatrix}^T$ denotes the end-position of the left and right legs in the sagittal and control directions.

Considering Eq. (7) in Cartesian space, we have:

$$\mathcal{M}_I \ddot{Y} + \mathcal{D}_I \dot{Y} + \mathcal{K}_I = f_x \tag{14}$$

where

$$\mathcal{M}_I = \mathbb{M}_I J(q_r) \tag{15}$$

$$\mathcal{D}_I = \mathbb{D}_I J_{q_r} + \mathbb{M}_{[I]} \dot{J}(q_r) \tag{16}$$

$$\mathcal{K}_I = \mathbb{M}_I \ddot{q}_r - \mathbb{D}_I \dot{q}_r + \mathbb{K}_I \tag{17}$$

The position of the left and right hip in the sagittal direction, according to the end-position of the left and right leg X and the reference trajectory angle, is given as follows:

$$P_{rx}^H = P_{rx} - L_t \sin(q_{r1}) - L_s \sin(q_{r1} + q_{r2}) \tag{18}$$

$$P_{lx}^H = P_{lx} + L_t \sin(q_{r3}) + L_s \sin(q_{r3} + q_{r4}) \tag{19}$$

where P_{rx}^H and P_{lx}^H represent the positions of the right and left hip in the sagittal direction, respectively. L_s and L_t denote the lengths of the shank and thigh, respectively.

The position of Center of Mass (COM), denoted as $p_o = \begin{bmatrix} P_{xo} & P_{yo} \end{bmatrix}^T$, which is defined as midpoint of the hip, is given as follows:

$$\begin{cases} P_{xo} = \frac{P_{lx}^H + P_{rx}^H}{2} \\ P_{yo} = \beta \sin(\frac{\pi t}{\Gamma}) \end{cases} \tag{20}$$

where β and Γ are the positive constants. According Li et al. (2021) and Itadera et al. (2019), the position of Zero Moment-Point (ZMP) is given as follows:

$$p_z = \begin{cases} P_{xz} = P_{xo} - \frac{h_c}{g} \ddot{P}_{xo} \\ P_{yz} = P_{yo} - \frac{h_c}{g} \ddot{P}_{yo} \end{cases} \tag{21}$$

The position of the Zero Moment Point (ZMP), denoted as p_z, is determined based on the Eqs. (18) to (21). The ZMP represents the point on the ground where there is no moment exerted on the robot. The ZMP position p_z consists of P_{xz} and P_{yz}, which are obtained by adjusting the position of the COM (P_{xo} and P_{yo}) according to the height of the COM (h_c) and the gravitational acceleration (g). The changes in the measurable human–robot interaction force (f) can affect the ZMP, as discussed in Haldar and Pagar (2023).

In order to achieve stable walking under external forces, a set of ZMP positions (P_z) is determined to maintain the gait within the effective support region. By adjusting P_z in response to changes in the measurable force (f), the exoskeleton can ensure stable and dynamically balanced walking. By confining the applied force within certain bounds, the exoskeleton can maintain stability during walking.

2.4. Dynamic model and state equation of exoskeleton

The dynamic model of a lower limb exoskeleton, which describes its motion according to the principles of Newton–Euler, can be represented by the following equation:

$$M(q)\ddot{q} + V(q,\dot{q})\dot{q} + C(q)q + F_e(t) = T + T_f \tag{22}$$

where q, $\dot{q}$, and $\ddot{q} \in \mathfrak{R}^n$ represent the joint angle, joint angular velocity, and joint angular acceleration, respectively. The matrix $M(q) \in \mathfrak{R}^{n\times n}$ contains the mass and inertia elements. The vector $V(q,\dot{q}) \in \mathfrak{R}^n$ represents the centrifugal and Coriolis forces. The vector $C(q) \in \mathfrak{R}^n$ accounts for the gravitational forces. The vector $F_e(t) \in \mathfrak{R}^n$ denotes external disturbance forces. $T \in \mathfrak{R}^n$ represents the forces generated by the actuators, while T_f represents human–robot interaction force.

To obtain the state equation, we introduce the state vector $X = \begin{bmatrix} x_1 & x_2 \end{bmatrix}^T$, where $X_1 = q$ and $X_2 = \dot{x}_1 = \dot{q}$. Eq. (22) can then be rewritten as:

$$\begin{cases} \dot{X}_1 = X_2 \\ \dot{X}_2 = M^{-1}(q)[-V(q,\dot{q})X_2 - C(q)X_1 - F_e(t) + T + T_f] \end{cases} \tag{23}$$

The general dynamic model of the exoskeleton, represented by Eq. (22), can be expressed in the form of a state equation as follows:

$$\dot{X} = AX + Bu \tag{24}$$

where

$$A = \begin{bmatrix} 0 & 1 \\ -M^{-1}(q)C(q) & -M^{-1}(q)V(q,\dot{q}) \end{bmatrix} \tag{25}$$

$$B = \begin{bmatrix} 0 \\ 1 \end{bmatrix} \tag{26}$$

$$u = \begin{bmatrix} T + T_f - F_e \end{bmatrix} \tag{27}$$

where A and B are matrices that contains the system parameters, and u denotes the control input.

In this study, we employ a controller law given by the following equation:

$$u = K_p e + K_i \int_0^t e dt + K_d \frac{de}{dt} \tag{28}$$

where the controller parameters are represented as $K_p = diag[K_{p1}, \ldots, K_{Pn}] \in \mathfrak{R}^{n\times n}$, $K_i = diag[K_{i1}, \ldots, K_{in}] \in \mathfrak{R}^{n\times n}$, and $K_d = diag[K_{d1}, \ldots, K_{dn}] \in \mathfrak{R}^{n\times n}$. The term $e = diag[e_1, \ldots, e_n] \in \mathfrak{R}^{n\times n}$ denotes the steady-state error, which is defined as follows:

$$e = q - q_r \tag{29}$$

where $q_r = diag[q_{r1}, \ldots, q_{rn}] \in \mathfrak{R}^{n\times n}$ and $q = diag[q_1, \ldots, q_n] \in \mathfrak{R}^{n\times n}$ are the desired and actual angular trajectories for the hip and knee joints. To simplify notation, we introduce a new variable $\dot{Z}$, defined as the derivative of e with respect to time. Thus, we can rewrite Eq. (28) as follows:

$$u = K_p e + K_i Z + K_d \dot{e} \tag{30}$$

Theorem 1. *Stability of a Non-linear Continuous Function*

Consider a non-linear continuous function defined as follows:

$$y = f(x) \tag{31}$$

The function $f(x)$ is considered stable if there exists a positive-definite Lyapunov function $V(x)$ (Li and Yang, 2020).

For all x in the domain of $f(x)$, the Lyapunov function $V(x)$ should be positive-definite, meaning that $V(x)$ approaches values in the range $[0,\infty)$. This can be expressed as:

$$\forall x \in \mathbb{R}^n; \quad \exists V(x); \quad V(x) \to [0,\infty) \tag{32}$$

In addition, the time derivative of the Lyapunov function, denoted as $\dot{V}(x)$, must be negative-definite (Liu et al., 2020; Aliman et al., 2022). This implies that for all x in the domain of $f(x)$, there exists a Lyapunov function $V(x)$ such that $V(x)$ is positive-definite, $V(x) \to [0,\infty)$, and $\dot{V}(x)$ is negative-definite, $\dot{V}(x) \to (-\infty, 0]$.

$$\forall x \in \mathbb{R}^n; \quad \exists V(x); \quad V(x) \to [0,\infty); \quad \dot{V}(x) \in \mathbb{R}^n; \quad \dot{V}(x) \to (-\infty, 0] \tag{33}$$

A positive-definite solution P is assumed to exist for any given positive-definite matrix Q, satisfying the equation $PA + A^T P = -Q$, where A is the control matrix.

The Lyapunov candidate function is defined as follows:

$$V = X^T PX + \tilde{K}_p{}^T \Psi^{-1} \tilde{K}_p + \tilde{K}_i{}^T \Psi^{-1} \tilde{K}_i + \tilde{K}_d{}^T \Psi^{-1} \tilde{K}_d \tag{34}$$

where $\Psi > 0 \in R^{n \times n}$ represents the adaptive rate. The estimation errors of $\tilde{K}_p$, $\tilde{K}_i$, and $\tilde{K}_d$ are obtained by defining:

$$\tilde{K}_p = K_p - \hat{K}_p \tag{35}$$

$$\tilde{K}_i = K_i - \hat{K}_i \tag{36}$$

$$\tilde{K}_d = K_d - \hat{K}_d \tag{37}$$

where $\hat{K}_p$, $\hat{K}_i$, and $\hat{K}_d$ are the estimation of the controller parameters. The time derivative of Eq. (34) can be expressed as follows:

$$\dot{V} = \dot{X}^T PX + X^T P\dot{X} + \dot{\tilde{K}}_p^T \Psi^{-1} \tilde{K}_p + \tilde{K}_p{}^T \Psi^{-1} \dot{\tilde{K}}_p + \cdots$$

$$\ldots + \dot{\tilde{K}}_i^T \Psi^{-1} \tilde{K}_i + \tilde{K}_i{}^T \Psi^{-1} \dot{\tilde{K}}_i + \dot{\tilde{K}}_d^T \Psi^{-1} \tilde{K}_d + \tilde{K}_d{}^T \Psi^{-1} \dot{\tilde{K}}_d \tag{38}$$

where $\dot{\tilde{K}}_p$, $\dot{\tilde{K}}_i$, and $\dot{\tilde{K}}_d$ represent the time derivatives of $\tilde{K}_p$, $\tilde{K}_i$, and $\tilde{K}_d$, respectively. $\dot{X}^T$ is derived from state equation of dynamic model as given in Eq. (24). It is also assumed that $\dot{\tilde{K}}_p^T \Psi^{-1} \tilde{K}_p = \tilde{K}_p{}^T \Psi^{-1} \dot{\tilde{K}}_p$, $\dot{\tilde{K}}_i^T \Psi^{-1} \tilde{K}_i = \tilde{K}_i{}^T \Psi^{-1} \dot{\tilde{K}}_i$, and $\dot{\tilde{K}}_d^T \Psi^{-1} \tilde{K}_d = \tilde{K}_d{}^T \Psi^{-1} \dot{\tilde{K}}_d$. The time derivative of the Lyapunov function can be written as follows:

$$\dot{V} = X^T A^T PX + B^T uPX + X^T PAX + X^T PBu + \cdots$$

$$\ldots + 2\dot{\tilde{K}}_p^T \Psi^{-1} \tilde{K}_p + 2\dot{\tilde{K}}_i^T \Psi^{-1} \tilde{K}_i + 2\dot{\tilde{K}}_d^T \Psi^{-1} \tilde{K}_d \tag{39}$$

Also we can have,

$$\dot{V} = -X^T QX + (B^T PX + X^T PB)u + \cdots$$

$$\ldots + 2\dot{\tilde{K}}_p^T \Psi^{-1} \tilde{K}_p + 2\dot{\tilde{K}}_i^T \Psi^{-1} \tilde{K}_i + 2\dot{\tilde{K}}_d^T \Psi^{-1} \tilde{K}_d \tag{40}$$

By substituting Eq. (30) into Eq. (40), the time derivative of the Lyapunov function can be written as follows:

$$\dot{V} = -X^T QX + \tilde{K}_p (B^T PXe + X^T PBe + 2\dot{\tilde{K}}_p^T \Psi^{-1} \tilde{K}_p) + \cdots$$

$$\ldots + \tilde{K}_i (B^T PXZ + X^T PBZ + 2\dot{\tilde{K}}_i^T \Psi^{-1} \tilde{K}_i) + \cdots$$

$$\ldots + \tilde{K}_d (B^T PX\dot{e} + X^T PB\dot{e} + 2\dot{\tilde{K}}_d^T \Psi^{-1} \tilde{K}_d) \tag{41}$$

To ensure a negative-definite time derivative of the Lyapunov function $\dot{V} = -X^T QX$, satisfying Theorem 1, the expressions for $\dot{\tilde{K}}_p$, $\dot{\tilde{K}}_i$, and $\dot{\tilde{K}}_d$ are as follows:

$$\dot{\tilde{K}}_p = \frac{-\Psi B^T PXe - \Psi X^T PBe}{2} \tag{42}$$

$$\dot{\tilde{K}}_i = \frac{-\Psi B^T PXZ - \Psi X^T PBZ}{2} \tag{43}$$

$$\dot{\tilde{K}}_d = \frac{-\Psi B^T PX\dot{e} - \Psi X^T PB\dot{e}}{2} \tag{44}$$

Based on these equations, the controller parameters K_p, K_i, and K_d can be obtained by integrating the respective expressions over time and adding the unknown controller parameters $\acute{K}_p$, $\acute{K}_i$, and $\acute{K}_d$:

$$K_p = \int_0^t \dot{\tilde{K}}_p dt + \acute{K}_p \tag{45}$$

$$K_i = \int_0^t \dot{\tilde{K}}_i dt + \acute{K}_i \tag{46}$$

$$K_d = \int_0^t \dot{\tilde{K}}_d dt + \acute{K}_d \tag{47}$$

The values of the unknown parameters $\acute{K}_p$, $\acute{K}_i$, and $\acute{K}_d$ can be determined through an optimization problem to improved performance and reduced steady-state error of the closed-loop system.

2.5. SBAS optimization and initialization of controller parameters

To determine the unknown parameters, an optimization problem is defined based on tuning the closed-loop controller parameters, in which the controller parameters are design variables. The design variables are denoted as:

$$x = \begin{bmatrix} \acute{K}_p & \acute{K}_i & \acute{K}_d \end{bmatrix} \tag{48}$$

The aim of parameter optimization is to minimize the objective function, which is derived from the steady-state error. By considering the closed-loop function of the control system, the steady-state error of the objective function $e_{obj}(s)$ can be expressed as follows:

$$e_{obj}(s) = 1 - \frac{u(s)G_i(s)}{1 + u(s)G_i(s)} \tag{49}$$

where $G_k(s)$ represents the mathematical model of each joint, and $u(s)$ represents the controller. The objective function is defined as the sum of the absolute values of the steady-state errors over a given time period. It can be expressed as follows:

$$f(x) = \sum_{x=0}^{n} |e_{obj}(x)| \tag{50}$$

This objective function represents the cumulative error and quantifies the overall performance of the control system. The goal is to minimize this objective function by optimizing the controller parameters.

The SBAS is a meta-heuristic optimization method that belongs to the class of high-level, problem-independent algorithmic strategies for developing heuristic optimization algorithms (Abualigah et al., 2022). In comparison to other classical algorithms such as particle swarm optimization, genetic algorithm and ant colony optimization, SBAS offers distinct advantages in terms of its simplicity and enhanced search capability (Shao and Fan, 2021). Its simplicity enables ease of implementation, while its larger search ability enhances its effectiveness in exploring the solution space and finding optimal or near-optimal solutions. SBAS utilizes the physiological principle observed in predator beetles during their search for food. These beetles rely on their antennas to detect the strength of food odours when exploring unfamiliar locations. By measuring the intensity of the food odour pheromones using both their left and right antennas, they can determine the direction of the target food. For instance, when the right antenna detects a stronger pheromone than the left antenna, the beetle will move towards the right direction. Conversely, if the left antenna perceives a stronger pheromone, the beetle will move towards the left. This behaviour inspires the SBAS algorithm, where the position of the food to be found by the beetle corresponds to the optimal objective function value, and the beetle's position serves as the design variable of the objective function. Initially, the search direction is chosen arbitrarily in any dimension of space to explore the unknown environment. Hence, the SBAS algorithm defines the standard search direction as follows:

$$\vec{c} = \frac{a}{\|a\|} \tag{51}$$

$$a = \text{rand}(-1, 1, n) \tag{52}$$

where $\vec{c} \in \mathbb{R}^n$ denotes the unit vector representing the standardized searching dimension, $a \in \mathbb{R}^n$ represents a randomly generated value between -1 and 1, and n denotes the number of design variables considered as the searching dimensions in the SBAS algorithm. The positions of the right and left antennas can be determined as follows:

$$x_r = x_j^i + d^i \cdot \vec{c} \tag{53}$$

$$x_l = x_j^i - d^i \cdot \vec{c} \tag{54}$$

where i represents the iteration number, j denotes the population size, x_r and x_l represent the positions of the right and left antennas, respectively, and d^i corresponds to the searching diameter at iteration i. In this algorithm, the movement direction (left or right) is determined based on the odour intensity detected by the beetle. The position update for each step can be expressed as follows:

$$x_j^{i+1} = x_j^i + \lambda^i \cdot \vec{c} \cdot \text{sign}(f(x_l) - f(x_r)) + \omega^i \tag{55}$$

where λ^i represents the step size, $\vec{c}$ is the search direction, and ω^i denotes a searching bias. $f(x_l)$ and $f(x_r)$ are the objective function values for the left and right antenna positions, respectively. The sign function, denoted as sign(.), is defined as follows:

$$\text{sign}(f(x_l) - f(x_r)) = \begin{cases} 1, & \text{if } f(x_l) - f(x_r) > 0 \\ 0, & \text{if } f(x_l) - f(x_r) = 0 \\ -1, & \text{if } f(x_l) - f(x_r) < 0 \end{cases} \tag{56}$$

This determines whether the beetle moves to the left, stays in place, or moves to the right based on the comparison of the objective function values. The update equations for the searching diameter d, step size λ, and searching bias ω are as follows:

$$d^{i+1} = d^i + 0.95 \cdot d_o \tag{57}$$

$$\lambda^{i+1} = 0.95 \cdot \lambda^i \tag{58}$$

$$\omega^{i+1} = \omega^i + 0.95 \cdot \omega_o \tag{59}$$

where d_o and ω_o represent the initial values of the searching diameter and searching bias, respectively. These update equations control the convergence behaviour of the SBAS algorithm by gradually reducing the search diameter, step size, and searching bias over iterations. The objective function for beetle's position $f(x)$ is determined in each iteration. After evaluating the beetle's position in each population, the minimum value of the objective function is stored as $f_{\text{best}}(x)$. The update rule for $f_{\text{best}}(x)$ is as follows:

$$\begin{cases} \text{if } f(x)^{i+1} < f_{\text{best}}(x)^i : & f_{\text{best}}(x)^{i+1} = f(x)^{i+1} \\ \text{if } f(x)^{i+1} \geq f_{\text{best}}(x)^i : & f_{\text{best}}(x)^{i+1} = f_{\text{best}}(x)^i \end{cases} \tag{60}$$

This update rule ensures that the best objective function value found so far is retained in each iteration. If a new candidate solution has a lower objective function value, it replaces the previous best value; otherwise, the previous best value is kept. Ultimately, $f_{\text{best}}(x)$ represents the minimum objective function value achieved throughout the optimization process.

To determine the global best solution, the value of $f_{\text{best}}(x)$ is evaluated in each iteration. The $f_{\text{best}}(x)$ with the lowest value is considered as the global best $g_{\text{best}}(x)$, and its corresponding beetle position is stored as x_{best}.

The update rule for $g_{\text{best}}(x)$ and x_{best} is as follows:

$$\begin{cases} \text{if } f_{\text{best}}(x)^{i+1} < g_{\text{best}}(x)^i : & g_{\text{best}}(x)^{i+1} = f_{\text{best}}(x)^{i+1}, \quad x_{\text{best}}^{i+1} = x^{i+1} \\ \text{if } f_{\text{best}}(x)^{i+1} \geq g_{\text{best}}(x)^i : & g_{\text{best}}(x)^{i+1} = g_{\text{best}}(x)^i, \quad x_{\text{best}}^{i+1} = x_{\text{best}}^i \end{cases} \tag{61}$$

This update rule ensures that the best solution found by any beetle so far is compared with the global best solution. If a new beetle finds a better solution, both the global best solution ($g_{\text{best}}(x)$) and its corresponding position (x_{best}) are updated. Otherwise, the global best solution remains unchanged. Ultimately, $g_{\text{best}}(x)$ represents the best objective function value found among all the beetles, and x_{best} represents the corresponding beetle position. The optimal position of the beetle is recognized as the final result when the number of iterations reaches its maximum value:

$$\text{if } i = i_{\max} : \quad x_{\text{result}} = x_{\text{best}}^{i_{\max}} \tag{62}$$

where $i_{\max}$ represents the maximum number of iterations. where i_{max} is the maximum number of iterations. The result of SBAS is used for initialization of controller parameters for Eqs. (45), (46), and (47). This combination represents the novelty of ASIA, which will be validated in walking motion.

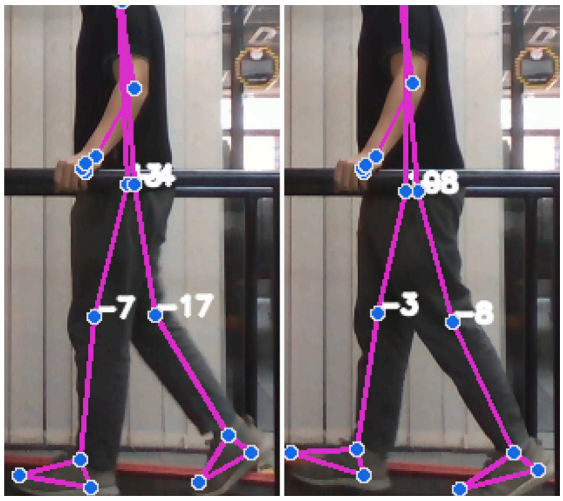

Fig. 7. Snapshot of camera frames for capturing the angular trajectory of walking motions by a healthy human subject.

3. Results and discussion

3.1. Experimental setup and data collection

The walking experiment was conducted to verify the performance of the proposed adaptive controller. The walking motions of a healthy human subject, aged 22 years old, male, height 171 cm, and weight 67 kg, were captured by an Intel® RealSense™ depth camera D435 to create desired angular trajectories for each joint. The captured trajectories were filtered by infinite impulse response and used as desired trajectories for the adaptive control system.

For the recording of the desired trajectories, we utilized the MediaPipe and OpenCV libraries in Python. These libraries provided the necessary tools for real-time motion tracking and visualization. Fig. 7 showcases some camera frames captured during the walking motion of the subject, demonstrating the data collection process.

Four healthy human subjects (subject 1: male, 22 years old, height 171 cm, weight 67 kg; subject 2: male, 34 years old, height 176 cm, weight 95 kg; subject 3: male, 54 years old, height 170 cm, weight 63 kg), and subject 4: female, 39 years old, height 160 cm, weight 88 kg wore the exoskeleton for testing of walking motion. They were required to walk on flat ground for 30 s.

3.2. Experimental and identified mathematical models

In this paper, the mathematical model of the exoskeleton's joints was established using system identification techniques based on previous studies by Amiri et al. (2020a), Amiri and Ramli (2022). The estimated mathematical model for each joint is represented as follows:

$$G_i(s) = \frac{\theta(s)}{u(s)} = \frac{b_i}{a_{j_i} s^3 + a_{j_i} s^2 + a_{j_i} s + a_{j_i}} \tag{63}$$

Table 3
Identified parameters for hip and knee joints.

	b_i	a_{1_i}	a_{2_i}	a_{3_i}	a_{4_i}
Hip ($i = 1$)	26.459	0.002	0.237	1.607	4.661
Knee ($i = 2$)	25.991	0.002	0.065	0.566	1.733

where $G_i(s)$ represents the mathematical model of the hip or knee joint. The parameters b_i and a_{j_i}, where $j = 1, 2, 3, 4$, correspond to the unknown parameters specific to each joint. For the hip joint, $i = 1$, and for the knee joint, $i = 2$. These parameters play a crucial role in characterizing the dynamics of the exoskeleton's joints. The parameters of the identified mathematical model for each joint have been displayed in Table 3, which have been obtained from previous studies conducted by Amiri et al. (2020a), Amiri and Ramli (2022).

These identified parameters provide a representation of the dynamics and characteristics of the hip and knee joints in the exoskeleton. They serve as inputs for the design and control of the exoskeleton, enabling precise motions. By incorporating these parameters into the control system, the exoskeleton can adapt to the user's movements and provide efficient and natural assistance during walking tasks.

We utilized Eq. (63) and the parameter values from Table 3 to define the mathematical model of each joint, denoted as $G_i(s)$, within the objective function $e_{obj(s)}$ as depicted in Eq. (49). The identified model was integrated into the closed-loop diagram of the ASIA controller, enabling the tuning of controller parameters using SBAS.

The controller parameters tuned by SBAS were $\acute{K}_p = \text{diag}[8.08, 6.73, 8.08, 6.73]$, $\acute{K}_i = \text{diag}[23.77, 21.36, 23.77, 21.36]$, and $\acute{K}_d = \text{diag}[1.16, 0.73, 1.16, 0.73]$. These values served as the initial parameter settings for the ASIA controller. Additionally, the parameters of the ASIA controller were designed as $\Psi = \text{diag}[0.5, 0.5, 0.5, 0.5]$ and $P = \text{diag}[2, 2, 2, 2]$. These parameters played a crucial role in regulating the control behaviour and response of the ASIA system.

In the trajectory tracking experiments, the healthy human subject participated by wearing the lower limb exoskeleton and performing separate repetitive walking exercises. The joints of the exoskeleton were actuated using DC motors operated in voltage control mode. These motors provided assistive force to the human hip and knee joints, while the joint angles were recorded using optical encoders connected to the motors for feedback. The experimental setup involved the subject wearing the exoskeleton and walking on a flat surface. Fig. 8 illustrates a snapshot of the four healthy human subjects wearing the exoskeleton and walking on flat ground for a duration of 30 s.

The walking trajectories of the lower limb exoskeleton's joints (LH, LK, RH, and RK) for healthy human subjects are as depicted in Fig. 9. Human healthy subjects 1, 2, 3, and 4 were required to walk on flat ground for 30 s. In these experiments the body dimension, gender, and age of the three human healthy subjects were different. These trajectories represented the desired joint angles (q_r) generated by the healthy human subject and applied as input to the adaptive controller. The actual trajectories (q) were obtained through the feedback of encoders connected to the actuators, capturing the real-time joint angles during the walking motion.

Fig. 9 demonstrates that the steady-state error e remained within a specific range, indicating the effectiveness of the proposed controller. Moreover, the actual trajectory closely tracked the desired trajectory, indicating accurate joint angle control. Furthermore, Fig. 10 illustrates the controller input u for each joint of the lower limb exoskeleton worn by the healthy human subjects.

In Fig. 10, the voltages applied to the actuators by the ASIA controller varied in response to changes in the angular trajectory. To validate the performance of the adaptive controller, another experiment was conducted using predefined periodically repeated desired trajectories as a comparison with (Amiri et al., 2020b), using a similar platform. Fig. 11 displays the angular trajectories of LH, LK, RH, and RK generated by the conventional PID controller.

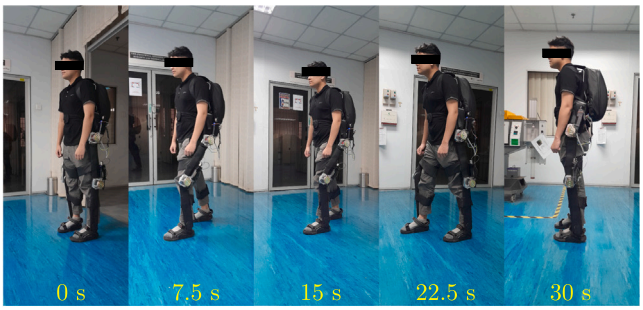

(a) subject 1: male, 22 years old, height 171 cm, weight 67 kg

(b) subject 2: male, 34 years old, height 176 cm, weight 95 kg

(c) subject 3: male, 54 years old, height 170 cm, weight 63 kg

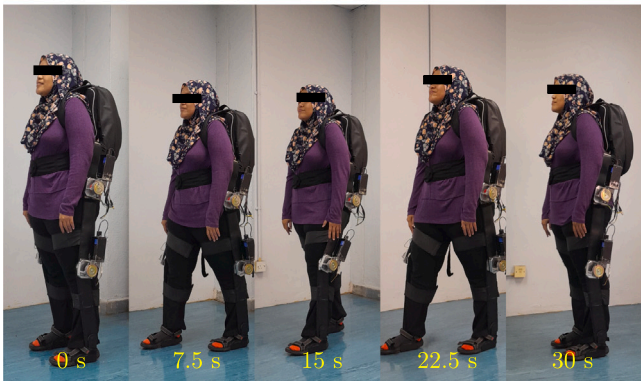

(d) subject 4: female, 39 years old, height 160 cm, weight 88 kg

Fig. 8. Snapshots of the healthy human subjects wearing the exoskeleton, while walking on the flat surface.

Table 4 provides a comparison of statistical analysis measurements including the maximum error (E_{max}), average error (E_{ave}), and Root Mean Square (RMS) for various controllers. This includes the ASIA

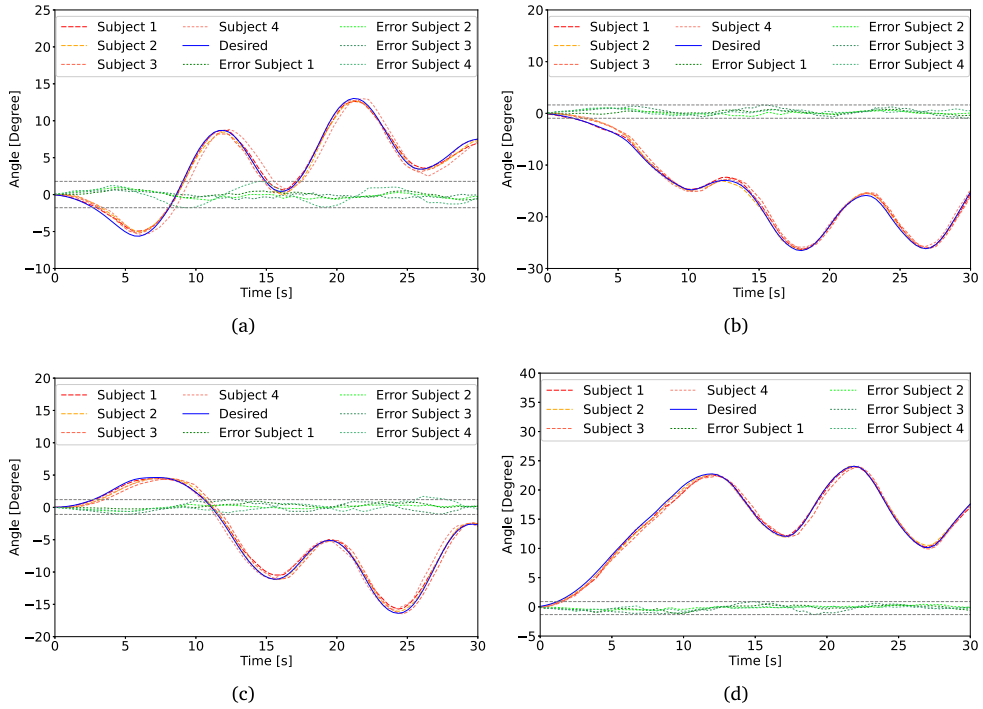

Fig. 9. Angular trajectory for LH, LK, RH, and RK of healthy human subjects.

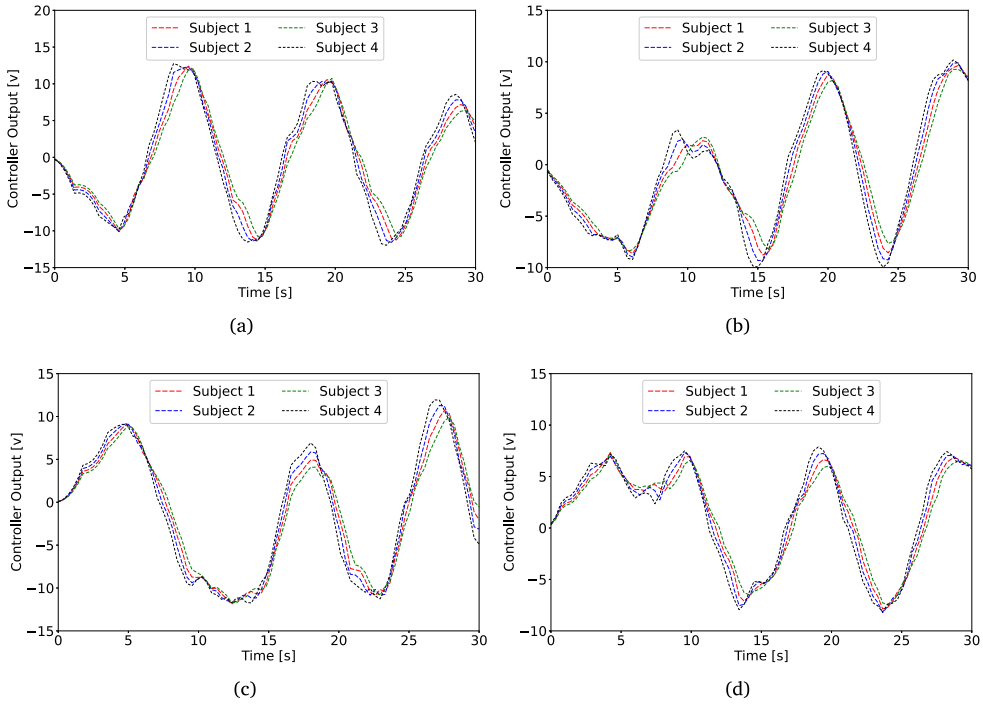

Fig. 10. Controller output for LH, LK, RH, and RK for healthy human subjects.

controller, PID controller from Amiri et al. (2020b), as well as the LAC, SFLC, and LASFC controllers from Amiri et al. (2022).

The performance of the proposed ASIA controller was compared with a conventional PID controller as well as other adaptive controllers including LAC, SFLC, and LASFC. The steady-state error analysis reveals that the ASIA controller achieves superior performance in trajectory tracking. For the LH joint, the ASIA controller exhibited a E_{max} of 0.032 rad, an E_{ave} of 0.011 rad, and an RMS of 0.013 rad. Similarly, for the LK, RH, and RK joints, the ASIA controller demonstrated low E_{max}, E_{ave}, and RMS values compared to the PID, LAC, SFLC, and LASFC controllers. Moreover, the ASIA controller demonstrated an average reduction of about 63% in E_{ave} compared to the PID controller, indicating its superior capability in minimizing the average error throughout the trajectory. Furthermore, when comparing the ASIA controller to other adaptive controllers, it consistently outperformed the LAC, SFLC, and LASFC controllers. The ASIA controller achieved an average reduction of approximately 57% in E_{max}, 66% in E_{ave}, and 53% in RMS compared to the LAC controller. Similarly, it demonstrates an average reduction of

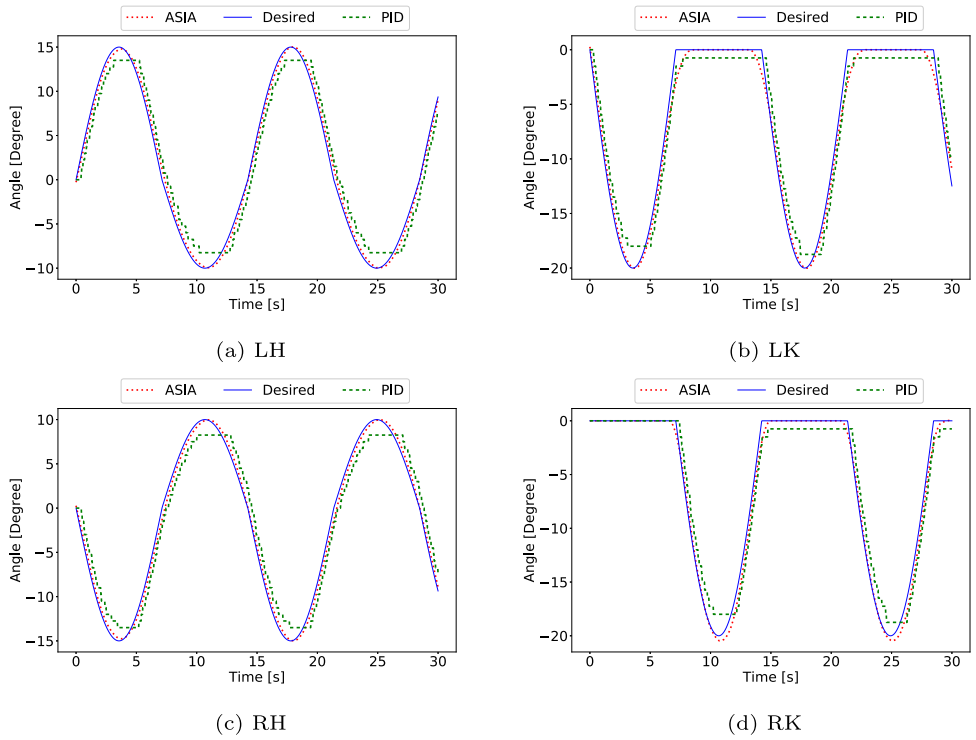

Fig. 11. Angular trajectory of LH, LK, RH, and RK for periodically repeated desired trajectories.

Table 4
Statistical comparison of the steady-state error for periodically repeated desired trajectories (radian).

Methods	Joints	E_{max}	E_{ave}	RMS	Joints	E_{max}	E_{ave}	RMS
ASIA	LH	0.032	0.011	0.013	LK	0.024	0.008	0 012
	RH	0.027	0.012	0.014	RK	0.027	0.007	0.013
PID	LH	0.048	0.029	0.030	LK	0.049	0.023	0.026
	RH	0.049	0.030	0.031	RK	0.052	0.019	0.024
LAC	LH	0.086	0.041	0.045	LK	0.1	0.045	0.058
	RH	0.084	0.040	0.042	RK	0.14	0.044	0.060
SFLC	LH	0.062	0.028	0.039	LK	0.078	0.038	0.047
	RH	0.060	0.024	0.035	RK	0.086	0.024	0.041
LASFC	LH	0.0477	0.013	0.029	LK	0.067	0.021	0.035
	RH	0.042	0.010	0.030	RK	0.074	0.013	0.037

about 44% in E_{max}, 53% in E_{ave}, and 52% in RMS compared to the SFLC controller. Additionally, when compared to the LASFC controller, the ASIA controller achieves an average reduction of approximately 37% in E_{max}, 48% in E_{ave}, and 35% in RMS. These significant percentage reductions in steady-state errors across all comparison scenarios underscored the superior performance of the ASIA controller in achieving accurate trajectory tracking. Overall, these results validate the effectiveness of the proposed ASIA controller in minimizing steady-state tracking errors during trajectory tracking experiments with periodically repeated desired trajectories.

In general, the experimental results clearly demonstrated the superior efficiency of the proposed ASIA controller compared to the methods presented in Amiri et al. (2022). The trajectory tracking experiments confirmed that the exoskeleton successfully follows the desired trajectories for the walking task, as generated by a healthy subject. Moreover, the analysis of steady-state error revealed that the ASIA controller effectively limits the error within a specific range, indicating its satisfactory performance. Overall, the experimental findings validate the effectiveness and robustness of the ASIA controller in achieving accurate trajectory tracking and ensuring desirable exoskeleton performance.

Table 5
Confusion matrix.

	Predicted stability	Predicted unsuitability
Actual stability	True Positive (TP) = 10	False Negative (FN) = 2
Actual unsuitability	False Positive (FP) = 3	True Negative (TN) = 5

In order to verify the validity of the ASIA controller on the exoskeleton for different patient specifics and gait patterns, a confusion matrix was used for 20 tests with different desired trajectories for the subjects (5 tests for each). The results for 20 experiments for 4 subjects have been given in Table 5. The TP, TF, FP, and TN are true positive, true negative, false positive and true negative, respectively.

In this test, the controller correctly predicted stability for 10 cases (TP) where the actual condition was stable; The controller predicted instability for 2 cases that were actually stable. The controller predicted stability for 3 cases that were actually unstable. The controller correctly predicted instability for 5 cases where the actual condition was unsuitable. The evaluation metrics for the confusion matrix is given as follows:

$$Accuracy = \frac{TP + TN}{TP + FN + FP + TN} = 0.714 \tag{64}$$

$$Precision = \frac{TP}{TP + FP} = 0.769 \tag{65}$$

$$Recall = \frac{TP}{TP + FN} = 0.833 \tag{66}$$

$$Specificity = \frac{TN}{TN + FP} = 0.625 \tag{67}$$

Based on the analysis of the confusion matrix and its associated performance metrics, it can be justified that the ASIA controller has been fine-tuned and customized to cater to diverse requirements and walking patterns.

4. Conclusion

This paper presents the gait trajectory controller based on the admittance swarm adaptive control system, which is combination of swarm-based intelligence, named SBAS with a Lyapunov-based adaptive controller, ASIA for a wearable lower limb exoskeleton. The ASIA controller was developed to overcome the human–robot interaction forces that were applied by the wearer to the walking exoskeleton.

The effectiveness of the ASIA controller performance was verified with different age, body dimensions and gender of healthy human subjects within the same conditions. The comparison results demonstrated the effectiveness of the proposed ASIA approach in terms of trajectory tracking accuracy and steady-state error.

This research contributes to the field of lower limb exoskeleton control by providing an effective and robust control approach that can enhance the functionality and usability of exoskeletons in assisting human movement for a walking task. The limitation of this work was the exoskeleton structure, which did not have adjustable links. This limitation did not permit us to test the controller with more diverse human subjects with significantly different body dimensions. In addition, the hardware used was in the affordable range. This resulted in faults that could affect the efficiency and accuracy of the experiments. In future work, the fault terms generated by the hardware can be considered in the dynamic model of the exoskeleton. Apart from the fault tolerance model a disturbance observer can be integrated with the control system to overcome unknown disturbances generated by the environment and the walking surface.

Declaration of competing interest

The authors declare that they have no known competing financial interests or personal relationships that could have appeared to influence the work reported in this paper.

Acknowledgement

The authors would like to thank Universiti Kebangsaan Malaysia (UKM) for the financial support received under Dana Impak Perdana research grant DIP-2022-005.

References

Abualigah, L., Elaziz, M.A., Khasawneh, A.M., Alshinwan, M., Ibrahim, R.A., Al-qaness, M.A.A., Mirjalili, S., Sumari, P., Gandomi, A.H., 2022. Meta-heuristic optimization algorithms for solving real-world mechanical engineering design problems: A comprehensive survey, applications, comparative analysis, and results. Neural Comput. Appl. 34 (6), 4081–4110. http://dx.doi.org/10.1007/s00521-021-06747-4.

Aliman, N., Ramli, R., Haris, S.M., Amiri, M.S., Van, M., 2022. A robust adaptive-fuzzy-proportional-derivative controller for a rehabilitation lower limb exoskeleton. Eng. Sci. Technol. Int. J. 35, 101097. http://dx.doi.org/10.1016/j.jestch.2022.101097.

Amiri, M.S., Ramli, R., 2022. Offline tuning mechanism of joint angular controller for lower-limb exoskeleton with adaptive biogeographical-based optimization. Turk. J. Electr. Eng. Comput. Sci. 30 (4), 1654. http://dx.doi.org/10.55730/1300-0632.3871.

Amiri, M.S., Ramli, R., Aliman, N., 2022. Adaptive swarm fuzzy logic controller of multi-joint lower limb assistive robot. Machines 10 (6), 425. http://dx.doi.org/10.3390/machines10060425.

Amiri, M.S., Ramli, R., Ibrahim, M.F., 2020a. Genetically optimized parameter estimation of mathematical model for multi-joints hip–knee exoskeleton. Robot. Auton. Syst. 125, 103425. http://dx.doi.org/10.1016/j.robot.2020.103425.

Amiri, M.S., Ramli, R., Tarmizi, M.A.A., Ibrahim, M.F., Danesh Narooei, K., 2020b. Simulation and control of a six degree of freedom lower limb exoskeleton. Jurnal Kejuruteraan 32 (2), 197–204. http://dx.doi.org/10.17576/jkukm-2020-32(2)-03.

Celesti, A., Cimino, V., Naro, A., Portaro, S., Fazio, M., Villari, M., Calabró, R.S., 2023. Recent considerations on gaming console based training for multiple sclerosis rehabilitation. Med. Sci. 10 (1), http://dx.doi.org/10.3390/medsci10010013.

Cho, J., Choi, D., Park, J.H., 2023. Sensorless variable admittance control for human-robot interaction of a dual-arm social robot. IEEE Access 11, http://dx.doi.org/10.1109/ACCESS.2023.3292933.

Cortese, M., Cempini, M., De Almeida, R., Paulo, R., Soekadar, S.R., Carrozza, M.C., Vitiello, N., 2015. A mechatronic system for robot-mediated hand telerehabilitation. IEEE/ASME Trans. Mechatronics 20 (4), 1753–1764. http://dx.doi.org/10.1109/TMECH.2014.2353298.

Daachi, M.E., Madani, T., Daachi, B., Djouani, K., 2015. A radial basis function neural network adaptive controller to drive a powered lower limb knee joint orthosis. Appl. Soft Comput. 34, 324–336. http://dx.doi.org/10.1016/j.asoc.2015.04.034.

Gallagher, J.F., Sivan, M., Levesley, M., 2022. Making best use of home-based rehabilitation robots. Appl. Sci. 12 (4), 1–15. http://dx.doi.org/10.3390/app12041996.

Guo, Q., Chen, Z., Yan, Y., Xiong, W., Jiang, D., Shi, Y., 2022. Model identification and human-robot coupling control of lower limb exoskeleton with biogeography-based learning particle swarm optimization. Int. J. Control Autom. Syst. 20 (2), 589–600. http://dx.doi.org/10.1007/s12555-020-0632-1.

Haldar, A.I., Pagar, N.D., 2023. Predictive control of Zero Moment Point (ZMP) for terrain robot kinematics. Mater. Today: Proc. 80, 122–127. http://dx.doi.org/10.1016/j.matpr.2022.10.286.

Itadera, S., Dean-Leon, E., Nakanishi, J., Hasegawa, Y., Cheng, G., 2019. Predictive optimization of assistive force in admittance control-based physical interaction for robotic gait assistance. IEEE Robot. Autom. Lett. 4 (4), 3609–3616. http://dx.doi.org/10.1109/LRA.2019.2928770.

Jiang, S., You, H., Zhao, W., Zhang, M., 2019. Effects of short-term upper limb robot-assisted therapy on the rehabilitation of sub-acute stroke patients. Technol. Health Care 29 (2), 295–303. http://dx.doi.org/10.3233/THC-202127.

Joel, J.P.A., Raj, R.J.S., Muthukumaran, N., 2022. Review on gait rehabilitation training using human adaptive mechatronics system in biomedical engineering. In: International Conference on Computer Communication and Informatics. pp. 1–5. http://dx.doi.org/10.1109/ICCCI54379.2022.9740794.

Khadidos, O.A., Alshareef, M.A., Manoharan, H., Khadidos, O.A., Shitharth, S., 2023. Application of improved support vector machine for pulmonary syndrome exposure with computer vision measures. Curr. Bioinform. 18, http://dx.doi.org/10.2174/1574893618666230206121127.

Lee, H.G., Wheeler, M.A., Quintana, F.J., 2022. Function and therapeutic value of astrocytes in neurological diseases. Nat. Rev. Drug Discov. 21 (5), 339–358. http://dx.doi.org/10.1038/s41573-022-00390-x.

Li, W., Liu, K., Li, C., Sun, Z., Liu, S., Gu, J., 2022. Development and evaluation of a wearable lower limb rehabilitation robot. J. Bion. Eng. 19 (3), 688–699. http://dx.doi.org/10.1007/s42235-022-00172-6.

Li, X., Yang, X., 2020. Lyapunov stability analysis for nonlinear systems with state-dependent state delay. Automatica 112, 108674. http://dx.doi.org/10.1016/j.automatica.2019.108674.

Li, Z., Zhao, K., Zhang, L., Wu, X., Zhang, T., Li, Q., Li, X., Su, C.Y., 2021. Human-in-the-loop control of a wearable lower limb exoskeleton for stable dynamic walking. IEEE/ASME Trans. Mechatronics 26 (5), 2700–2711. http://dx.doi.org/10.1109/TMECH.2020.3044289.

Liao, H., Chan, H.H.-T., Gao, F., Zhao, X., Liu, G., Liao, W.-H., 2022. Proxy-based torque control of motor-driven exoskeletons for safe and compliant human-exoskeleton interaction. Mechatronics 88, 102906. http://dx.doi.org/10.1016/j.mechatronics.2022.102906.

Liu, S., Liberzon, D., Zharnitsky, V., 2020. Almost Lyapunov functions for nonlinear systems. Automatica 113, 108758. http://dx.doi.org/10.1016/j.automatica.2019.108758.

Liu, Q., Liu, Y., Zhu, C., Guo, X., Meng, W., Ai, Q., Hu, J., 2021. Design and control of a reconfigurable upper limb rehabilitation exoskeleton with soft modular joints. IEEE Access 9, 166815–166824. http://dx.doi.org/10.1109/ACCESS.2021.3136242.

Metzger, J.C., Lambercy, O., Califfi, A., Dinacci, D., Petrillo, C., Rossi, P., Conti, F.M., Gassert, R., 2014. Assessment-driven selection and adaptation of exercise difficulty in robot-assisted therapy: A pilot study with a hand rehabilitation robot. J. NeuroEng. Rehabil. 11 (1), 1–14. http://dx.doi.org/10.1186/1743-0003-11-154.

Mujica, M., Crespo, M., Benoussaad, M., Junco, S., Fourquet, J.-Y., 2023. Robust variable admittance control for human–robot co-manipulation of objects with unknown load. Robot. Comput.-Integr. Manuf. 79, 102408. http://dx.doi.org/10.1016/j.rcim.2022.102408.

Pulloquinga, J.L., Escarabajal, R.J., Vallés, M., Díaz-Rodríguez, M., Mata, V., Vicente, Á., 2023. Admittance controller complemented with real-time singularity avoidance for rehabilitation parallel robots. Mechatronics 94, 103017. http://dx.doi.org/10.1016/j.mechatronics.2023.103017.

Sabbahi, A., Canada, J.M., Babu, A.S., Severin, R., Arena, R., Ozemek, C., 2022. Exercise training in cardiac rehabilitation: Setting the right intensity for optimal benefit. Prog. Cardiovasc. Dis. 70, 58–65. http://dx.doi.org/10.1016/j.pcad.2022.02.001.

Shao, X., Fan, Y., 2021. An improved beetle antennae search algorithm based on the elite selection mechanism and the neighbor mobility strategy for global optimization problems. IEEE Access 9, 137524–137542. http://dx.doi.org/10.1109/ACCESS.2021.3117567.

Singh, S., Kumar, M., Kumar, A., Shitharth, B.K.V.S., 2023. Pneumonia detection with QCSA network on chest X-ray. Sci. Rep. 13 (1), http://dx.doi.org/10.1038/s41598-023-35922-x, 1-16.

Sun, W., Lin, J.W., Su, S.F., Wang, N., Er, M.J., 2021. Reduced adaptive fuzzy decoupling control for lower limb exoskeleton. IEEE Trans. Cybern. 51 (3), 1099–1109. http://dx.doi.org/10.1109/TCYB.2020.2972582.

Takebayashi, T., Takahashi, K., Okita, Y., Kubo, H., Hachisuka, K., Domen, K., 2022. Impact of the robotic-assistance level on upper extremity function in stroke patients receiving adjunct robotic rehabilitation: Sub-analysis of a randomized clinical trial. J. NeuroEng. Rehabil. 19 (1), 1–10. http://dx.doi.org/10.1186/s12984-022-00986-9.

Wang, T., Chenhao, B.Z.L., Liu, T., Han, Y., Ferreira, S.W.J.P., Dong, W., Zhang, X., 2022. A review on the rehabilitation exoskeletons for the lower limbs of the elderly and the disabled. Electronics 11 (3), 1–16. http://dx.doi.org/10.3390/electronics11030388.

Wang, Y.H., Liu, G.Y., Huang, G., Wang, Y., 2023. Variable admittance force feedback device and its human-robot interaction stability. Robot. Comput.-Integr. Manuf. 82, 102537. http://dx.doi.org/10.1016/j.rcim.2023.102537.

Wu, Q., Chen, Y., 2023. Variable admittance time-delay control of an upper limb rehabilitation robot based on human stiffness estimation. Mechatronics 90, 102935. http://dx.doi.org/10.1016/j.mechatronics.2022.102935.

Wu, Q., Xingsong, W., Bai, C., Hongtao, W., 2018. Development of an RBFN-based neural-fuzzy adaptive control strategy for an upper limb rehabilitation exoskeleton. Mechatronics 53, 85–94. http://dx.doi.org/10.1016/j.mechatronics.2018.05.014.

Xu, J., Chen, X., Tan, Y., Zou, W., 2023. Robust admittance control with complementary passivity. IEEE Control Syst. Lett. 7, 2239–2244. http://dx.doi.org/10.1109/LCSYS.2023.3286812.

Zhang, L., Guo, S., Xi, F., 2023. Performance-based assistance control for robot-mediated upper-limbs rehabilitation. Mechatronics 89, 102919. http://dx.doi.org/10.1016/j.mechatronics.2022.102919.